

## Electronic Supplementary Information (ESI)

### Time-Dependent Photoemission from Droplets: Influence of Size and Charge on the Photophysics Near the Surface

Loren Ban,<sup>\*a</sup> Hanchao Tang,<sup>a</sup> Bruce L. Yoder<sup>a</sup> and Ruth Signorell<sup>\*a</sup>

---

<sup>a</sup> Department of Chemistry and Applied Biosciences, ETH Zürich, Vladimir-Prelog Weg 2, CH-8093 Zürich, Switzerland.

\* lban@ethz.ch, rsignorell@ethz.ch

## 1. Experimental methods

The experimental setup used in this work consists of an air-side configuration to prepare the aerosol sample and a droplet photoelectron spectrometer. We describe the aerosol sample preparation in Section 1.1, followed by the description of the droplet photoelectron spectrometer in Section 1.2. Finally, in Section 1.3 we describe the laser setup employed for droplet photoionization.

### 1.1. Aerosol sample preparation

The aerosol is prepared by atomization of liquid bis(2-ethylhexyl) phthalate (DEHP) and bis(2-ethylhexyl) sebacate (DEHS) mixtures in a Collision-type atomizer (Model 3076, TSI Inc.). An Aerodynamic Aerosol Classifier (AAC, Cambustion Ltd.) is used to size-select the aerosol droplets based on their aerodynamic diameter ( $D_a$ )<sup>1</sup>. The size-selected aerosol sample then enters the charge conditioning stage. Neutral aerosol samples were generated by an electrostatic precipitator (ESP) operated at 4.5 kV which removes charged droplets from the aerosol flow. Positively and negatively charged aerosol samples were generated by replacing the ESP by a corona-wire unipolar charger. The charging process is described by the continuum charging theory<sup>2</sup> (and references therein) and the degree of charging can be tuned by controlling the discharge current. After leaving the charge conditioning stage, the aerosol flow is split in two parts. The first part is for droplet size and concentration measurements performed in parallel to the photoionization experiment. This was achieved by using either a Scanning Mobility Particle Sizer (SMPS, Model 3938, TSI Inc.) spectrometer or only a Condensation Particle Counter (CPC, Model 3775, TSI Inc.). The second part of the aerosol flow was directed to the photoelectron spectrometer and is discussed in detail in the following section.

### 1.2. Photoelectron spectrometer

Part of the aerosol flow enters the photoelectron spectrometer through the Aerodynamic Lens (ADL), designed based on refs. 3–5 which transmits a wide range of particle diameters in the submicrometer range. The ADL has been employed in our previous studies<sup>6–9</sup>. In short, the transfer to vacuum is achieved by aerodynamically guiding the aerosol flow through a flow-limiting aperture ( $\varnothing 150 \mu\text{m}$ ) and a series of circular orifices. A scroll pump connected to the ADL entrance provides the ability to tune the flow rate through the ADL. The pressure is lowered from atmospheric in front of the ADL to  $\sim 10^{-4}$  mbar in the source chamber, at the exit of the ADL. In the source chamber, the gas flow is efficiently pumped away by two turbomolecular pumps (2300 L/s and 1200 L/s), while the droplets form a beam in vacuum at the exit of the ADL. The droplet beam passes through a skimmer ( $\varnothing 3 \text{ mm}$ , Beam Dynamics Inc.) and enters the differential pumping chamber ( $\sim 10^{-6}$  mbar, 500 L/s turbomolecular pump), before entering the photoelectron spectrometer chamber through an aperture ( $\varnothing 8 \text{ mm}$ ). The photoelectron chamber is kept at pressures  $< 10^{-6}$  mbar with a 500 L/s turbomolecular pump.

The photoelectron spectrometer consists of the electron extraction optics (repeller R, extractor E and ground G), the imaging detector (microchannel plate MCP, phosphorous screen PS) and a kHz camera<sup>7,10,11</sup>. Photoelectrons were generated by laser photoionization ( $h\nu_{1,2}$ ) and accelerated to the detector by applying voltages  $V_R$  and  $V_E$  to the repeller (R) and extractor (E), respectively. The spectrometer was operated in the Velocity Map Imaging (VMI) configuration ( $V_E/V_R \sim 0.7$ ). Two different detection modes were used in this work. In Sections 3.1.-3.3., we used the camera to record angle-resolved photoelectron images. Photoelectron kinetic energy (eKE) spectra were retrieved by image reconstruction along the laser propagation axis<sup>11</sup> with MEVIR<sup>12</sup> and background-corrected by subtracting the measurement without the droplet beam. In Sections 3.4. and 4., we decoupled the current signal directly from the imaging detector and recorded electron time-of-flight

(eTOF) spectra to retrieve total photoelectron yields. Recording photoelectron yields required averaging over less laser shots to achieve reasonable signal-to-noise ratio and was therefore chosen as a method to perform pump-probe studies over a wide range of time delays (see below).

### 1.3. Laser setup and pump-probe scheme

The femtosecond laser (Astrella, Coherent) delivers 35 fs pulses centered at 795 nm (1.56 eV) at a repetition rate of 1 kHz. We used a portion of the laser output ( $\sim 3$  mJ) and directed it to the second and third harmonic generation setup (Femtokit, Eksma). The 2<sup>nd</sup> harmonic (3.1 eV) was generated by frequency doubling in a thin BBO crystal (type I) and was coupled out by a harmonic separator. The 3<sup>rd</sup> harmonic (4.7 eV) was generated by removing the harmonic separator and allowing for sum-frequency generation in a second thin BBO crystal (type I). Nominal duration of both pulses is  $<70$  fs. In both cases, the polarization was adjusted to lie parallel to the plane of the VMI detector by a pair of thin-film polarizers and a  $\lambda/2$  plate provided the ability to vary the pulse energy. Typically, we used pulse energies of  $\sim 100$   $\mu$ J (3.1 eV) and  $\sim 3$   $\mu$ J (4.7 eV). The laser beam diameter in the interaction region was set to  $\sim 3$  mm ( $1/e^2$ ) which leads to intensities of  $\sim 35$  GW/cm<sup>2</sup> (3.1 eV) and  $\sim 1$  GW/cm<sup>2</sup> (4.7 eV).

A second laser source was used to compare the effect of the pulse length on photoemission from droplets. The nanosecond laser (Quantel Ultra) delivers  $\sim 7$  ns pulses with an energy of 4.7 eV and a repetition rate of 20 Hz. Polarization was adjusted to lie in the plane of the VMI detector by a beamsplitter cube and the pulse power was varied by rotation of a  $\lambda/2$  plate situated upstream of the beamsplitter cube. We produced energies of about 50  $\mu$ J per pulse and the laser beam diameter in the interaction region was set to  $\sim 3$  mm ( $1/e^2$ ) which results in intensity of  $\sim 100$  kW/cm<sup>2</sup>.

The experiments were performed in two configurations. For single-pulse experiments each beam was guided to the VMI spectrometer where it intersected the droplet beam. In the femtosecond case, the spectrometer was operated at 1 kHz, matching the laser repetition rate. In the nanosecond case, the repetition rate was 20 Hz which leads to lower signal-to-noise ratio for similar data collection times.

For the pump-probe experiments, the nanosecond and femtosecond beams were recombined and spatially overlapped in the VMI spectrometer with a nearly co-linear geometry. The instrument response function (IRF) is assumed to be equal to the time profile of the nanosecond pulse. Control of the pump-probe time delay and pulse synchronization was achieved through a delay generator (DG645 by SRS, rms jitter  $<40$  ps). The trigger signal from the femtosecond laser was sent through a home-built pulse skipper and every 50<sup>th</sup> pulse was sent to the delay generator. The pump-probe delay was then controlled through the delay generator by adjusting the nanosecond laser flash lamp trigger signal. The maximum pump-probe delay is limited to the distance between the two femtosecond pulses (1 ms). However, the droplet beam travels at a velocity of  $\sim 100$  m/s<sup>13</sup> which further constrains the maximum delay range to a time required for a droplet to transverse the laser beam profile. Assuming a laser beam diameter of 3 mm ( $1/e^2$ ), this would limit the maximal pump-probe delay to about 30  $\mu$ s.

## 2. Theoretical methods

DFT Calculations were performed with Gaussian 09<sup>14</sup>. We chose the functional and the basis set by comparing vertical ionization energies (VIE) and electronic energy levels of benzene<sup>15–17</sup> and benzoic acid<sup>18</sup> to values found in literature. Good agreement (within a few 100 meV) was obtained with the B3LYP functional and 6-311++G(d,p) basis set. Excited states were calculated with time-dependent (TD) DFT using the same basis set, but a slightly better agreement with literature was found with the CAM-B3LYP functional. After establishing a reasonable calculation procedure, we performed calculations on DBP.

The energy of the optimal ground state structure was taken as a reference energy level. The adiabatic singlet-triplet energy gap was calculated by geometry optimization of the lowest triplet state and equals 3.2 eV. The optimized ground and triplet state structures of DBP are shown in Figure 1. Vertical absorption spectra in the singlet and triplet manifolds were obtained from TD-DFT calculations at the optimal ground or triplet state geometries, respectively.

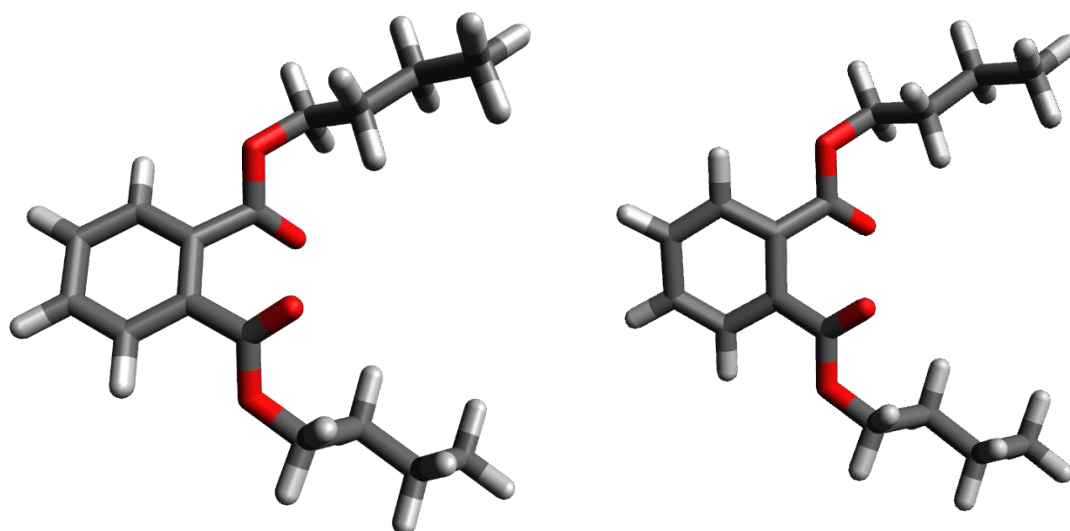


Figure 1 Optimal structures of the DEHP ground state (left) and lowest energy triplet state (right).

The VIE was calculated from a difference of energies of the optimal singlet (or triplet) neutral molecule and energy of the cationic state at the same geometry. As a rough estimation of the droplet environment, we also calculated the condensed phase VIE by using a polarizable continuum model (PCM) and benzene as a solvent as it has a very similar dielectric constant as DEHP and DEHS. We expect this rough approximation to be acceptable since the condensed phase shift of the VIE is in major part determined by the electrostatic stabilization of the ionic state. The values are summarized in Table 1.

Table 1 Calculated VIE for the ground and lowest triplet states of DEHP. Liquid values are approximated by a simple PCM model in benzene as the solvent. VIE: vertical ionization energy; AIE: adiabatic ionization energy.

	VIE (gas) / eV	AIE (gas) / eV	VIE (liquid) / eV	AIE (liquid) / eV
$S_0$	9.0	8.6	8.1	7.8
$T_1$	6.3	5.5	5.4	4.6

### 3. Total electron yield decay dynamics

An example of the recorded electron time-of-flight (eTOF) traces is shown in Figure 2.

At negative (panel a) and positive (panel b) time delays, the eTOF traces (dashed lines) contain two peaks which are separated by  $\Delta t$ . The peak at  $\Delta t = 0 \mu\text{s}$  is the nanosecond-pump signal, while the peak at time  $\Delta t$  corresponds to the femtosecond-probe signal. By comparing the nanosecond peak at negative and positive time delays one can see no probe-induced signal.

The background subtraction is greatly simplified by the fact that the pump and probe eTOF peaks are clearly separated in time. However, this is not valid at  $\Delta t \sim 0$  where both peaks overlap (panel b). To remove the single-pulse ns-pump background from the measurement (dashed lines) we used the eTOF trace recorded at a large  $\Delta t \sim 4 \mu\text{s}$ . Such a trace is shown as a dotted line and contains only the contributions of the single-pulse pump ionization.

The background-subtracted eTOF trace (dashed line – dotted line) is shown as a full line and it contains no contributions from the ns-pump, only the fs-probe. The same procedure is repeated for all time delays. Now it becomes apparent that the background-subtracted signal increases significantly at positive time delays (ns-pump first, panels b and c) compared to the negative time delay (fs-probe first, panel a), which directly illustrates the measured pump-probe signal.

Time-dependent electron yields  $Y(\Delta t)$  were extracted from the eTOF traces by integrating the background-subtracted traces in the region around the fs-probe peak. Finally, to correct for the single-pulse fs-probe background, the electron yields were subtracted by the corresponding value at the negative time delay (panel a,  $\Delta t = -30 \text{ ns}$ ).

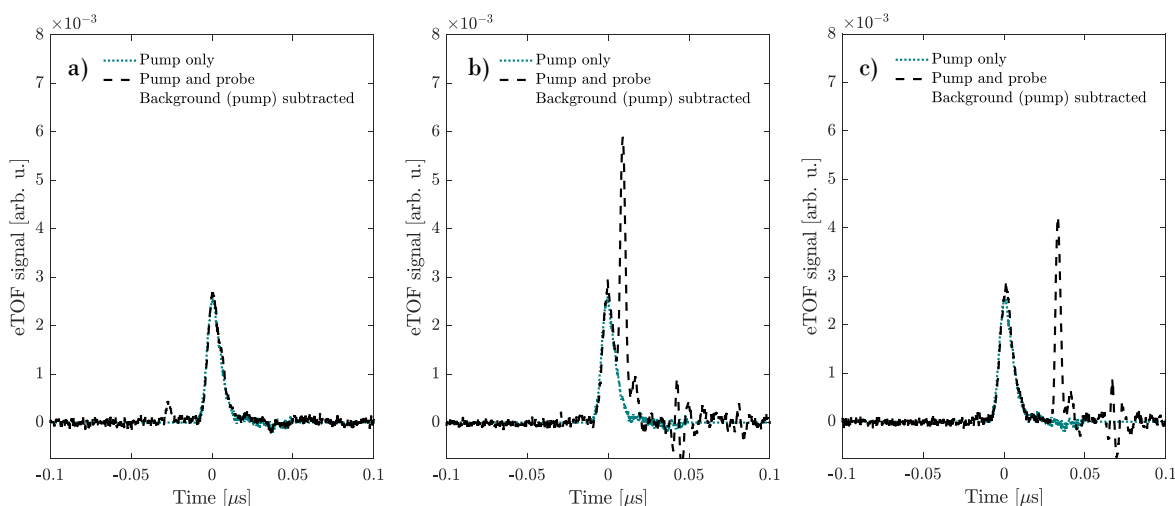


Figure 2 Electron time-of-flight traces for the nanosecond-femtosecond pump-probe experiment. Dashed lines show the measured eTOF trace at a given time delay, dotted lines show a background trace which includes contributions from the nanosecond pump only and full lines are the background-corrected traces where the nanosecond pump signal contribution is removed. a) eTOF trace at negative time delay with the femtosecond pulse (3.1 eV) interacting with the droplet first. b) eTOF trace at a time delay of 10 ns. c) eTOF trace at time delay of about 30 ns, where the clear pump probe signal is visible.

## References

- 1 F. Tavakoli and J. S. Olfert, *Aerosol Sci. Technol.*, 2013, **47**, 916–926.
- 2 C. Zheng, Q. Chang, Q. Lu, Z. Yang, X. Gao and K. Cen, *Aerosol Air Qual. Res.*, 2016, **16**, 3037–3054.
- 3 X. Wang and P. H. McMurry, *Aerosol Sci. Technol.*, 2006, **40**, 320–334.
- 4 X. Wang, F. E. Kruis and P. H. McMurry, *Aerosol Sci. Technol.*, 2005, **39**, 611–623.
- 5 X. Zhang, K. A. Smith, D. R. Worsnop, J. L. Jimenez, J. T. Jayne, C. E. Kolb, J. Morris and P. Davidovits, *Aerosol Sci. Technol.*, 2004, **38**, 619–638.
- 6 R. Signorell, M. Goldmann, B. L. Yoder, A. Bodi, E. Chasovskikh, L. Lang and D. Luckhaus, *Chem. Phys. Lett.*, 2016, **658**, 1–6.
- 7 S. Amanatidis, B. L. Yoder and R. Signorell, *J. Chem. Phys.*, 2017, **146**, 224204.
- 8 L. Ban, T. E. Gartmann, B. L. Yoder and R. Signorell, *Phys. Rev. Lett.*, 2020, **124**, 13402.
- 9 M. Goldmann, J. Miguel-Sánchez, A. H. C. West, B. L. Yoder and R. Signorell, *J. Chem. Phys.*, 2015, **142**, 224304.
- 10 T. E. Gartmann, S. Hartweg, L. Ban, E. Chasovskikh, B. L. Yoder and R. Signorell, *Phys. Chem. Chem. Phys.*, 2018, **20**, 16364–16371.
- 11 L. Ban, B. L. Yoder and R. Signorell, *Annu. Rev. Phys. Chem.*, 2020, **71**, 315–334.
- 12 B. Dick, *Phys. Chem. Chem. Phys.*, 2014, **16**, 570–580.
- 13 J. T. Jayne, D. C. Leard, X. Zhang, P. Davidovits, K. A. Smith, C. E. Kolb and D. R. Worsnop, *Aerosol Sci. Technol.*, 2000, **33**, 49–70.
- 14 M. J. Frisch, G. W. Trucks, H. B. Schlegel, G. E. Scuseria, Ma. Robb, J. R. Cheeseman, G. Scalmani, V. Barone, B. Mennucci, G. A. Petersson and others, *Gaussian 09 (Revision D. 01)*, Wallingford CT, 2013.
- 15 E. C. Da Silva, J. Gerratt, D. L. Cooper and M. Raimondi, *J. Chem. Phys.*, 1994, **101**, 3866–3887.
- 16 A. Nenov, S. Mukamel, M. Garavelli and I. Rivalta, *J. Chem. Theory Comput.*, 2015, **11**, 3755–3771.
- 17 R. E. Stratmann, G. E. Scuseria and M. J. Frisch, *J. Chem. Phys.*, 1998, **109**, 8218–8224.
- 18 J. Li, F. Zhang and W.-H. Fang, *J. Phys. Chem. A*, 2005, **109**, 7718–7724.